Crystallographic orientation dependence of mechanical properties in the superelastic Ti-24Nb-4Zr-8Sn alloy

H. Jabir, A. Fillon,* P. Castany, and T. Gloriant
Université Rennes, INSA Rennes, CNRS, ISCR - UMR 6226, F-35000 Rennes, France

(Received 6 June 2018; published 18 June 2019)

Nanoindentation and electron backscattered diffraction techniques are used to study the dependence of crystallographic orientation on mechanical properties in individual grains of the superelastic polycrystalline Ti-24Nb-4Zr-8Sn alloy. Strain recovery, elastic modulus, and hardness are evaluated from the force-displacement curves using spherical and Berkovich indenters. Experimental data are reported in a standard stereographic triangle covering all possible crystallographic directions of loading in the bcc-β structure of the Ti-24Nb-4Zr-8Sn alloy. Our experiments show that both spherical and Berkovich indenters are suitable for probing anisotropy of elastic modulus whereas spherical indenter is more appropriate for probing anisotropy of superelastic response. The highest indentation strain recovery is measured along $\langle 001\rangle_\beta$ and the lowest one is observed along $\langle 111\rangle_\beta$. Our inverse pole figure distribution of indentation strain recoveries is in good agreement with inverse pole figure distribution of compressive lattice distorsions calculated from the crystallographic model of martensitic transformation in β titanium alloys. This established pattern in compression is very different from that seen during tensile deformation, and both our experiments and calculations confirm the strong tension-compression asymmetry of the strain response in superelastic β titanium alloys. The indentation modulus also shows significant crystallographic anisotropy: $E_{[001]\beta} < E_{[101]\beta} < E_{[111]\beta}$. In contrast, orientation dependence is lost when plasticity has set in, and hardness becomes independent of crystallographic orientation due to the fact that multiple directions are prone to generate slip systems in the bcc-β structure.

DOI: 10.1103/PhysRevMaterials.3.063608

I. INTRODUCTION

In the last 20 years, titanium based alloys entirely composed of nontoxic and nonallergenic β-stabilizing elements have been the focus of much attention especially in view of their adequate biocompatibility and more suitable elastic behavior for use in biomedicine when compared to other metallic biomaterials [1–6]. β-stabilizer alloying elements (Nb, Ta, Mo, Zr, and Sn) lower the allotropic transformation temperature of titanium and stabilize the β phase, which retains the more compliant bcc structure. Ti alloys with predominance of this phase offer a lowering in elastic modulus, without sacrificing their strength and toughness making them the most promising metallic materials for hard tissue substitutes [7–13]. For a narrow range of β-stabilizer equivalent concentrations, the metastable β phase can be retained to room temperature after quenching from the β phase field. Metastable β Ti alloys may present superelastic behavior associated with a stress-induced and reversible martensitic transformation [14–19], which make them highly desirable for the fabrication of biomedical smart devices such as cardiovascular stents, guide wires for catheters, drills for root canal procedures, and orthodontic arch wires [20–23]. Superelasticity arises from mechanical instability of the metastable β phase that turns into nonequilibrium α'' martensite (orthorhombic phase) on loading and reverts back to β phase on unloading resulting in a remarkable and unusual strain recovery for metallic alloys.

The effect of alloying elements and influence of thermomechanical processing on mechanical properties of metastable β Ti alloys have been extensively investigated in the literature [24–29]. It is confirmed that phase composition, grain size, and texture of metastable β Ti alloys impact their superelastic performances and mechanical properties [30–36]. Beyond this, the uniaxial deformation behavior of single crystals of metastable β Ti alloys displays crystallographic anisotropy: (i) regarding superelasticity, crystals along the $\langle 101\rangle_\beta$ direction provide the highest recoverable strain and crystals along $\langle 111\rangle_\beta$ the lowest one during tensile testing, (ii) the lowest elastic modulus is observed along the $\langle 001\rangle_\beta$ direction and the highest one along $\langle 111\rangle_\beta$. These experimental results are in accordance with theoretical calculations for these both properties [10,37–39]. A good understanding of orientation-dependent mechanical response in superelastic Ti alloys will help to determine preferential structural features to approach optimum performance for specific application. Over the last decade, micro- and nanoscale mechanical testing, including mostly micropillar compression tests and nanoindentation tests have become more widely employed in order to understand the local mechanical response of materials [40–50]. In the case of the most popular superelastic Ni-Ti alloy system, nanoindentation testing on individual grains with various crystal orientations have revealed mechanical anisotropy mainly driven by anisotropy of the stress-induced formation of martensite [47–50]. It is supposed that lattice distorsion strains involved during martensitic transformation

*Corresponding author: amelie.fillon@insa-rennes.fr

to accommodate the applied strain, are strongly dependent on the crystallographic direction of loading [51]. According to our knowledge, no experimental data exists on the orientation dependence of the superelastic response in individual grains of polycrystalline metastable β Ti alloys. A thorough understanding of the superelastic response, elastic modulus, and hardness in individual grains with regards to their orientation is of great interest to optimize initial structural features in order to achieve the desired mechanical behavior for relevant application.

The present study focuses on the polycrystalline metastable β Ti-24Nb-4Zr-8Sn alloy (composition in wt. %; abbreviated as Ti2448), which has been designed by Hao *et al.* for use primarily in biomedicine [8,9]. The present work uses strategy initiated in a previous work combining electron backscattered diffraction (EBSD) analysis for identifying grain orientations and nanoindentation measurements for exploring elastic and plastic responses of individual grains depending on their orientation [40]. Measured data are reported in inverse pole figures that have the advantage of displaying the value distribution of each measured property in a single representation for all possible crystallographic directions of loading. In this way, depth-recovery, elastic modulus, and hardness, all measured during nanoindentation in individual grains of the polycrystalline metastable β Ti2448 alloy are successively reported in a standard stereographic triangle covering all possible normal surface directions (also loading directions). Results show a full experimental study of orientation-dependent indentation response in the metastable β Ti2448 alloy covering all crystallographic directions of loading and allowing a full evaluation of changes in superelastic and elastic responses. Experimental results are discussed and interpreted in relation to the crystallographic model of martensitic transformation in metastable β Ti alloys.

II. MATERIALS AND METHODS

A slice of a hot-forged cylinder of Ti2448 alloy is used as raw material in this work [8]. The slice is directly multipass cold rolled to a reduction rate of 40%. The cold rolled specimen is then solution treated under high vacuum at 900 °C for 30 min followed by water quenching to retain the metastable β phase at room temperature. This specific thermomechanical treatment is choosen to produce an optimal initial microstructure with random texture and appropriate grain size for easily probing a wide range of crystal orientations. Chemical analyses are performed in a scanning electron microscope (SEM) attached with an energy dispersive x-ray spectroscopy system (EDXS). Results show that the solution treated Ti2448 alloy consists of 23.9% Nb, 4.1% Zr, 8.2% Sn, and Ti at balance (wt. %), in agreement with the nominal composition. The phase composition of the solution treated alloy is analyzed on a Rigaku x-ray diffraction (XRD) system with Co K_α radiation at 30 kV and 20 mA. Microstructure analysis is carried out on a JEOL JSM 6400 SEM equipped with TSL electron backscattered diffraction system which is used in this work to identify crystallographic orientation of individual grains. Prior to EBSD analysis, the sample surface is carefully prepared by polishing with several SiC abrasive papers down to a mesh size of 4000, followed by a final polishing with a colloidal silica suspension of 0.02 μm. Lastly, chemical etching in 5% HNO_3, 5% HF, and 90% H_2O solution (vol. %) is performed during a few seconds to remove the thin work-hardened surface layer and to reveal the microstructure. A low surface roughness (Ra) below 9 nm has been measured in the region of interest by atomic force microscopy in tapping mode evidencing the high quality surface finish that is absolutely crucial for the fulfillment of both EBSD analysis and subsequent nanoindentation measurements. After determining the crystallographic orientation of each grain over large area, the local mechanical properties of individual grains are evaluated from nanoindentation experiments. To achieve this, individual grains with labeled orientation are located using an optical microscope coupled with the instrumented NHT CSM nanoindentation test system. Load controlled nanoindentation tests are performed along the surface normal direction of selected grains, at room temperature, using two kinds of indenters: a spherical diamond tip with nominal radius of 50 μm and a modified Berkovich diamond tip ($\alpha \approx 65.31°$). Standard calibrations of indenter tips (indenter area functions and load frame compliances) have been performed on fused silica. In this study, each indentation experiment is carried out at a fixed maximum load of 30 mN with the spherical tip and 10 mN with the Berkovich tip. Berkovich indentations are carried out in grains for which diameter is at least 40 μm and spherical indentations are conducted in grains with diameters of more than 80 μm. Nanoindentation measurements are limited to the central region of each selected grain to avoid any influence of grain boundaries and previous surrounding indentation experiments, thus reflecting the actual behavior of single crystals along a defined crystal direction. Elastic modulus and hardness values are extracted from a nanoindentation unloading curve using the equivalent indenter Oliver and Pharr method [52]. A minimum of five nanoindentation measurements are performed in individual grains with similar orientations to assert the reproductibity of results. Moreover, the random texture we designed allows exhaustive and statiscally representative measurements for a very wide range of grain orientations. In the case of superelastic alloys, it is recognized that recoverable depth after nanoindentation test, which is defined as the difference between h_{max}, the depth at maximum load (F_{max}), and h_r, the remnant depth upon complete unloading (Fig. 1), is associated with the sum of usual elastic recovery and superelastic recovery [43,53]. To characterize the superelastic effect, the recovery ratio under nanoindentation is evaluated from the force-displacement curve by measuring the depth-recovery ratio as shown in Fig. 1 and following the relation:

$$\varepsilon_{rec} = (h_{max} - h_r)/h_{max}. \quad (1)$$

It is commonly accepted that higher the depth-recovery ratio ε_{rec}, the greater the superelastic effect [43,53]. Another approach to gauge the superelastic effect is to analyze the mechanical work done during the loading-unloading process. The total work done during loading can be separated into two parts: the irrecoverable energy W_{irrec}, which is mainly due to plastic deformation during indentation experiment and corresponds to area enclosed by both loading and unloading curves, and the recoverable energy W_{rec}, which refers to area below unloading curve (Fig. 1). Hence the energy dissipation

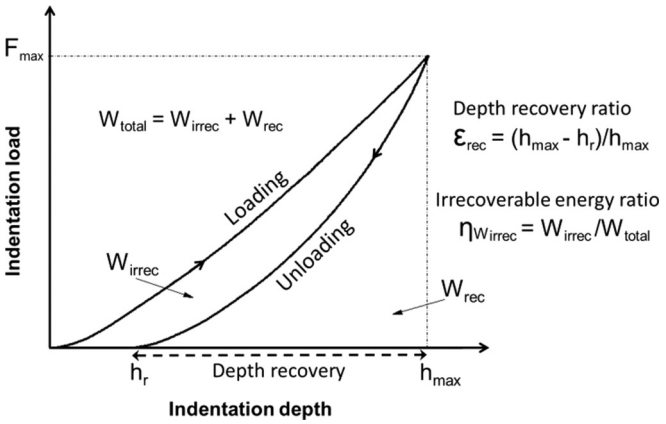

FIG. 1. Schematic illustration of load-displacement curve during nanoindentation experiment. Definition of the depth-recovery ratio $\varepsilon_{\rm rec}$ and the irrecoverable energy ratio $\eta_{\rm Wirrec}$ established from the parameters h_r, $h_{\rm max}$, $W_{\rm irrec}$, and $W_{\rm rec}$ read on the graph.

ratio is determined as

$$\eta_{\rm Wirrec} = W_{\rm irrec}/W_{\rm total}, \tag{2}$$

and is a key parameter inversely related to the superelastic contribution. It is reported that the irrecoverable energy ratio $\eta_{\rm Wirrec}$ is weakened in superelastic alloys by contribution of the reversible martensitic transformation [43,53]. Therefore, a smaller $\eta_{\rm Wirrec}$ indicates that a large amount of transformed martensite reverses back into β during unloading.

III. RESULTS AND DISCUSSION

A. Microstructure

XRD pattern of solution treated Ti2448 alloy is obtained in θ-2θ symmetric geometry at room temperature (Fig. 2). The diffraction profile displays the main reflections (110), (200), (211), (220) corresponding to the polycrystalline bcc β-Ti structure. The corresponding lattice parameter of β phase is calculated to be 0.3298 nm, which is consistent with results previously published for Ti2448 alloy [17]. The

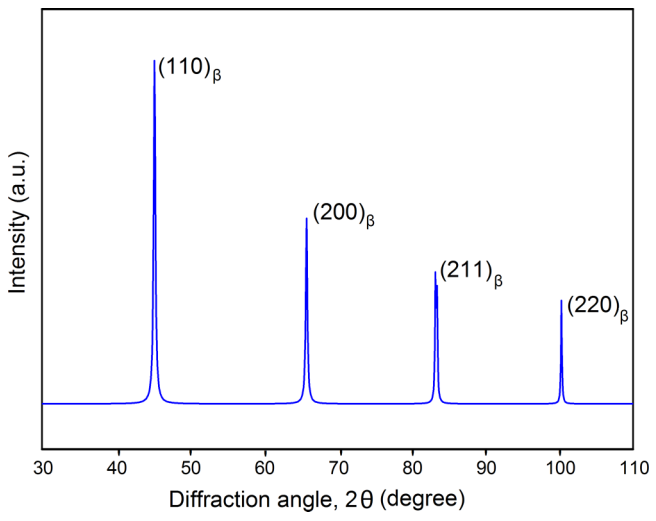

FIG. 2. XRD profile of the solution treated Ti2448 alloy.

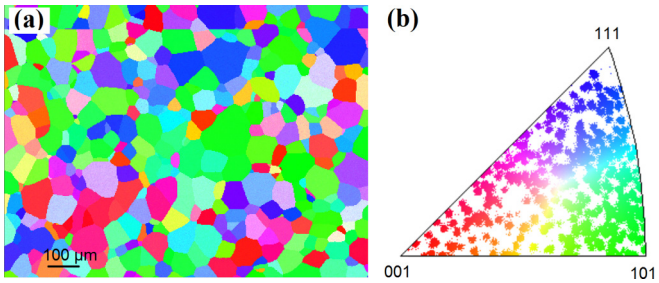

FIG. 3. (a) EBSD orientation map of the solution treated Ti2448 alloy. (b) Corresponding orientation distribution of surface normals (also the loading directions) of individual grains in the standard stereographic triangle for β phase.

EBSD orientation map in a selected region of our Ti2448 alloy is presented in Fig. 3(a). As shown, the microstructure of the solution treated Ti2448 reveals equiaxed β grains with an average size of 80 μm. Thus, preliminary observations show a fully recrystallized β phase microstructure. Measured orientations along normal surface direction are reported in the standard stereographic triangle for the β phase [Fig. 3(b)] and clearly show the polycrystalline and randomly textured bcc microstructure. The analyzed area consists of several hundered of grains that cover the entire inverse pole figure subsequently allowing the fulfilment of an exhaustive mechanical study along all possible crystallographic directions (also the loading directions).

B. Superelastic deformation in individual grains

1. Nanoindentation load-displacement curves for the three principal crystallographic directions

Figure 4 displays nanoindentation results into selected grains with indentation directions close to $\langle 001\rangle_\beta$, $\langle 101\rangle_\beta$ or $\langle 111\rangle_\beta$ orientations with maximal deviation of 18° from each principal direction. Typical load-displacement curves obtained with the spherical tip are presented on the one hand [Fig. 4(a)], and those measured with a Berkovich tip, on the other hand [Fig. 4(b)]. Note that data presented on these graphs are normalized in relation to the maximum measured load $F_{\rm max}$ for the Y axis and to the maximum measured depth $h_{\rm max}$ for the X axis. This procedure is applied for each indentation experiment. Mean values of depth-recovery ratios $\langle\varepsilon_{\rm rec}\rangle$ and those of irrecoverable energy ratios $\langle\eta_{\rm Wirrec}\rangle$ are also provided in Fig. 4 for each principal direction. Maximum penetration depths, regardless of the grain orientation, range from 230 to 250 nm for spherical indentations at 30 mN maximum load and from 350 to 380 nm for Berkovich indentations at 10 mN maximum load (See Supplemental Material [54]).

Berkovich indentations differ from spherical indentations in three general aspects. The first aspect concerns the global shape of indentation curves, which displays a reduced final return when the Berkovich tip is used. This can be seen by restricted depth-recoveries and hence severely high remnant depths h_r (the complementary part) with normalized h_r values between 0.71 and 0.76 after Berkovich indentations. In contrast, spherical indentations lead to remarkable extended depth

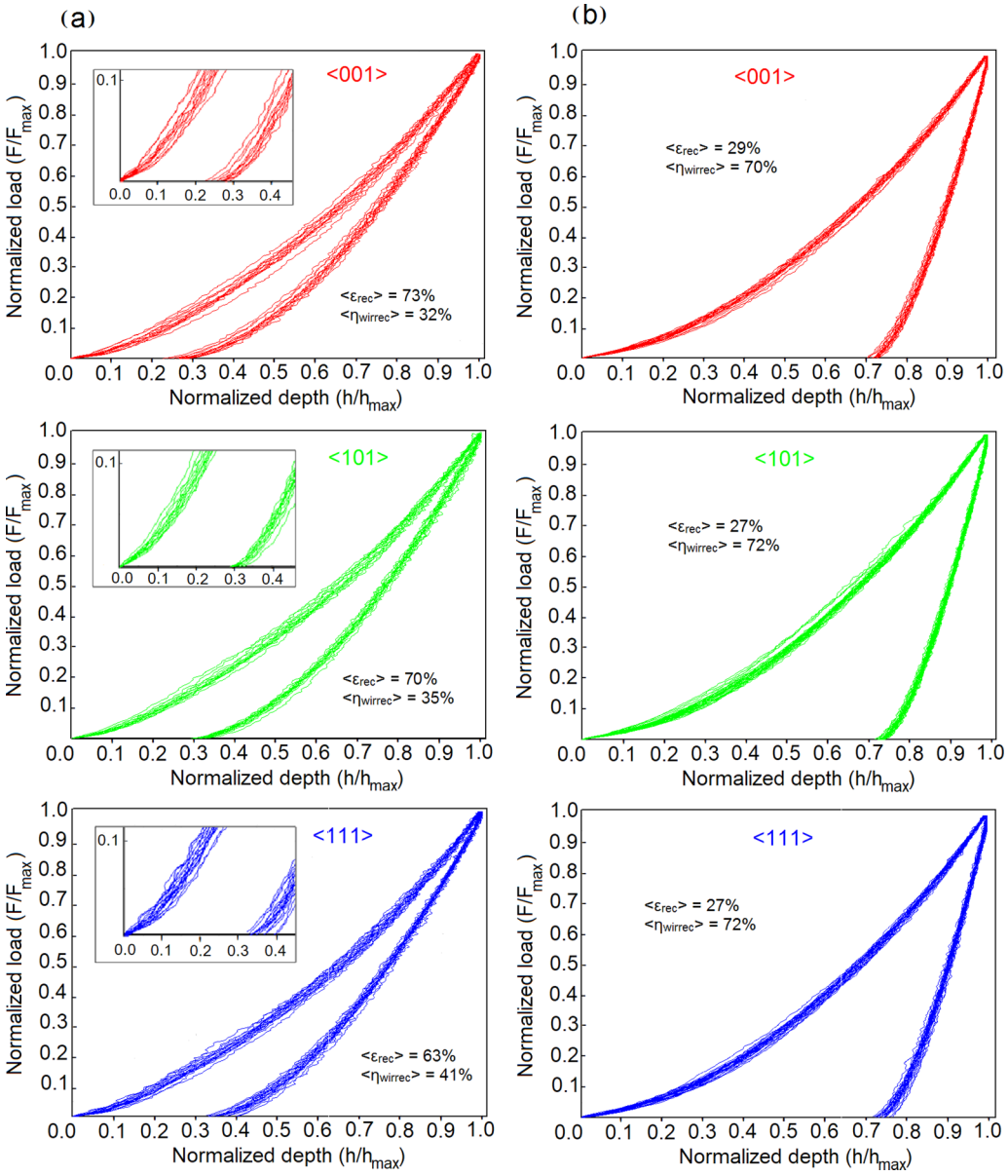

FIG. 4. Nanoindentation results of the Ti2448 alloy for grains close to $\langle 001\rangle_\beta$, $\langle 101\rangle_\beta$, and $\langle 111\rangle_\beta$ orientations. Normalized load–displacement curves measured with the spherical tip at $F_{\max} = 30$ mN (a) and with Berkovich tip at $F_{\max} = 10$ mN (b). For each nanoindentation experiment, the continuously measured loads and depths are, respectively, normalized to the measured $F_{\max}$ and to the measured $h_{\max}$.

recoveries and hence considerably smaller normalized h_r values contained in the interval 0.24–0.40. The second point to mention is about dissipated energy W_{irrec} upon indentation experiment: observed W_{irrec} associated with the Berkovich tip is much wider than it is for the spherical tip (Fig. 4). This is evidenced by mean values of irrecoverable energy ratios $\langle \eta_{\text{Wirrec}} \rangle$, which are very high under Berkovich tip in the range of 70%–72%, and extremely reduced with the spherical tip in the range of 32%–41%. Berkovich indentations are associated with sudden and immediate onset of plasticity causing extremely steep unloading curves. There is singularity at the tip of Berkovich indenter that produces large stresses. Plastic deformation becomes thus the predominant deformation mechanism during Berkovich nanoindentations that do not provide ideal situation to probe the superelastic nature of the Ti2448 alloy. In contrast, spherical indentations exhibit the softest slopes on the unloading curves evidencing greater ease for reversible strain accommodation. It is generally observed that the depth- and energy-recovery ratios are lower for sharp indenters like Berkovich than for spherical indenters. A significant volume of material immediately underneath the Berkovich tip is so highly strained that most of the deformation is accommodated by dislocation slip rather than by indentation-induced phase transformation, inhibiting superelastic recovery upon unloading [53,55,56]. When significant deformation occurs by dislocation motion, the superelastic effect is deteriorated. The use of a Berkovich indenter is thus not the best configuration to probe reversible straining in superelastic alloys, while spherical indenters facilitate the reversible deformation [57] and allow us to further differentiate fine changes in strain recovery with crystallographic orientation.

The third issue is to emphasize the influence of crystallographic loading direction on load-displacement curves. Normalized indentation curves from the Berkovich tip do not indicate at first sight any noticeable change related to crystal directions. Mean depth-recovery ratios $\langle\varepsilon_{rec}\rangle$ measured along each principal crystallographic direction fall into a very narrow range of values (27%–29%) with the Berkovich tip meaning that normalized remnant depths h_r seem independent of crystallographic loading directions [Fig. 4(b)]. In contrast, spherical indentations highlight significant scattering in the $\langle\varepsilon_{rec}\rangle$ results between the three principal crystallographic directions: $\langle\varepsilon_{rec}\rangle$ is measured as 73%, 70%, and 63% for loading directions close to $\langle 001\rangle_\beta$, $\langle 101\rangle_\beta$, and $\langle 111\rangle_\beta$, respectively. This trend can clearly be seen on close-up views of Fig. 4(a) with an obvious move in the scatter band of normalized h_r depending on the principal direction. It is worth noting that measured $\langle\varepsilon_{rec}\rangle$ mean values are very reproducible for each principal direction with small mean standard deviations 1.2%, 0.8%, and 1.6%, respectively, for the $\langle 001\rangle_\beta$, $\langle 101\rangle_\beta$, and $\langle 111\rangle_\beta$ directions. $\langle\varepsilon_{rec}\rangle$ fluctuations depending on the principal direction extend beyond mean standard deviations with the spherical tip evidencing that the force-displacement response of our material depends on the cristallographic loading direction. This is also evidenced by the mean values of $\langle\eta_{Wirrec}\rangle$ representing the dissipating energy ratio measured as 32%, 35%, and 41% for loading directions close to $\langle 001\rangle_\beta$, $\langle 101\rangle_\beta$, and $\langle 111\rangle_\beta$, respectively. Therefore, spherical indentations reveal a distinct mechanical response of the metastable β Ti2448 alloy depending on the crystallographic loading direction.

2. *Anisotropy of the indentation strain recovery* ε_{rec}

For a more detailed representation of crystallographic anisotropy of superelastic response in the metastable β Ti2448 alloy, indentation strain recovery ratios ε_{rec} measured in individual grains with spherical and Berkovich indenters are reported in a standard stereographic triangle for a wide selection of crystallographic loading directions. The corresponding inverse pole figure (IPF) distributions of indentation strain recovery ratios (ε_{rec}-IPF) for the two indenter geometries are then presented in Fig. 5. The position of each point in stereographic triangle corresponds to the normal direction of the indented grain and its color refers to the measured value

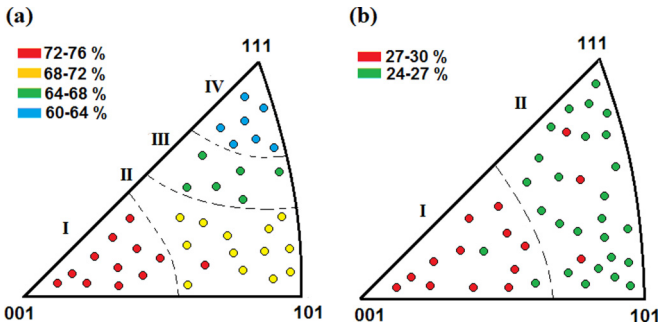

FIG. 5. Inverse pole figure distribution of indentation strain recoveries (ε_{rec}-IPF) measured with spherical tip (a) and with Berkovich tip (b).

of ε_{rec} in the center of the grain according to provided color scale. Each colored point corresponds to the average of at least five measurements and the mean standard deviation is 1.5%. ε_{rec} is a key parameter used in the present study to investigate recoverable deformation behavior. Clearly, ε_{rec} values change according to crystal orientation. Maximum values of ε_{rec} are found around $\langle 001\rangle_\beta$ orientation for both indenters. Nevertheless, ε_{rec} measured from spherical indentations regardless of the grain orientation show a larger scattering (from 60% to 76%) than those measured from Berkovich indentations (from 24 to 30%) in accordance with the comments from the previous section. ε_{rec}-IPF obtained with the Berkovich tip in Fig. 5(b) can be divided into two regions. Region I focuses around $\langle 001\rangle_\beta$ orientation and exhibits maximum ε_{rec} values (27%–30%). Region II shows very slight decline of ε_{rec} values (24%–27%). Berkovich ε_{rec} values remain considerably low and do not show any relevant sign of crystallographic dependency because during Berkovich indentations plastic deformation predominates and deteriorates the superelastic effect [53,55,56]. ε_{rec}-IPF obtained with the spherical tip in Fig. 5(a) shows a wide dispersion of ε_{rec} values from 60 to 76 %. The high statistic of measurements carried out along a wide selection of crystallographic orientations corroborates the fact that significant evolution of spherical ε_{rec} values exists with crystal orientation. Maximum and minimum spherical ε_{rec} distribute, respectively, around $\langle 001\rangle_\beta$ and $\langle 111\rangle_\beta$ orientations. ε_{rec}-IPF can be divided into four distinct regions. Region I around the $\langle 001\rangle_\beta$ direction has the highest spherical ε_{rec} value in the range 72%–76%, region IV around the $\langle 111\rangle_\beta$ direction has the lowest spherical ε_{rec} value in the range 60%–64%, regions II and III have spherical ε_{rec} values falling in the intermediate interval (64%–72%). These high ε_{rec} values show that reversible deformation mechanisms remain predominant during spherical nanoindentation. It is well known that spherical indenters can produce a smooth transition from elastic to elastic-plastic contact. It has been shown that extensive plastic deformation can be easily avoided and so superelasticity can be readily assessed by using a spherical indenter [53,55–57]. The large difference in the magnitude of indentation strain ratios ε_{rec} between the spherical and Berkovich indenters confirm that the relative amount of elastic and plastic deformation (strain distribution) induced beneath the indenter tip is very different for the two indenter geometries [53,55,56]. One interesting finding that emerges from the study of ε_{rec}-IPF is that spherical nanoindentation offers a suitable means to probe crystallographic anisotropy of strain recovery. Recoverable deformation is only due to elastic deformation in conventional materials, while it is expected in superelastic alloys that an additional and important contribution from the stress-induced martensitic transformation participates in the reversible straining as discussed in the next section.

3. *Theoretical anisotropy of the martensitic transformation strain* ε_M

The superelastic nature of the polycrystalline Ti2448 alloy is associated with a reversible martensitic transformation between the β phase and stress-induced α'' phase [17,58]. Indeed, the superelastic metastable β Ti alloys that the

TABLE I. Six lattice correspondence variants derived from the β-α" orientation relationship.

Variant	$[100]_{\alpha''}$	$[010]_{\alpha''}$	$[001]_{\alpha''}$
V1	$[100]_\beta$	$[011]_\beta$	$[0\bar{1}1]_\beta$
V2	$[100]_\beta$	$[0\bar{1}1]_\beta$	$[01\bar{1}]_\beta$
V3	$[010]_\beta$	$[101]_\beta$	$[10\bar{1}]_\beta$
V4	$[010]_\beta$	$[10\bar{1}]_\beta$	$[\bar{1}01]_\beta$
V5	$[001]_\beta$	$[110]_\beta$	$[\bar{1}10]_\beta$
V6	$[001]_\beta$	$[\bar{1}10]_\beta$	$[\bar{1}\bar{1}0]_\beta$

superelastic part of the recoverable strain, i.e., the accommodated strain from the martensitic transformation, is driven by geometric compatibilities between the β and α" phases in superelastic metastable β Ti alloys [16]. Six lattice correspondence variants *Vi* between the β (bcc) parent phase and α'' (C-centered orthorhombic) phase can be derived from the following orientation relationship: $[100]_{\alpha''} - \langle 100\rangle_\beta$ $[010]_{\alpha''} - \langle 011\rangle_\beta$ $[001]_{\alpha''} - \langle 0\bar{1}1\rangle_\beta$ (Table I). Figure 6 illustrates lattice correspondence between the β and α'' phases for the variant named *V5* in Table I. Lattice distorsions induced from transformation of the β phase to α'' phase can be calculated from the previous orientation relationship using the lattice constant of the parent β phase ($a_\beta = 0.3298$ nm) and those of the α'' phase measured *in situ* under stress ($a_{\alpha''} = 0.3195$ nm, $b_{\alpha''} = 0.4814$ nm, $c_{\alpha''} = 0.4730$ nm) in a previous work [57]. Lattice distortions along the three principal axes of the α'' crystal can then be calculated as $\eta_1 = \frac{a_{\alpha''}}{a_\beta} = 0.969$; $\eta_2 = \frac{b_{\alpha''}}{a_\beta\sqrt{2}} = 1.031$; $\eta_3 = \frac{c_{\alpha''}}{a_\beta\sqrt{2}} = 1.014$.

To go even further in this approach, a lattice distortion matrix $T^{(Vi)}$ can be expressed in the coordinates of the parent β phase for each martensite variant *Vi* [16,59]. As an example, lattice distorsion matrix $T^{(V5)}$ corresponding to variant *V5* presented on Fig. 6, is defined as follows:

$$T^{(V5)} = \begin{pmatrix} \frac{\eta_2+\eta_3}{2} & \frac{\eta_2-\eta_3}{2} & 0 \\ \frac{\eta_2-\eta_3}{2} & \frac{\eta_2+\eta_3}{2} & 0 \\ 0 & 0 & \eta_1 \end{pmatrix}. \quad (3)$$

This means that a vector x in coordinates of the β crystal will be transformed to $x'^{(Vi)}$ during martensitic transformation following the relation $x'^{(Vi)} = T^{(Vi)}x$. In this way, the lattice distorsion strain induced by martensitic transformation $\varepsilon_M^{(Vi)}$ can be expressed for each martensite variant *Vi* along any x

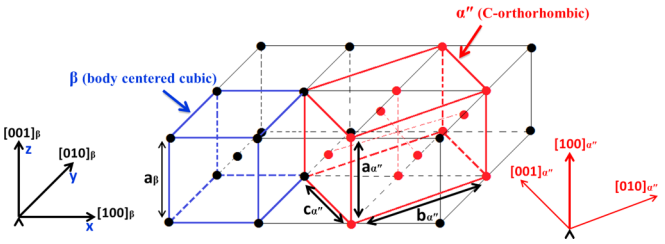

FIG. 6. Schematic illustration exhibiting lattice correspondence between parent β phase (bcc) and α" phase (C-centered orthorhombic) for the variant *V5*.

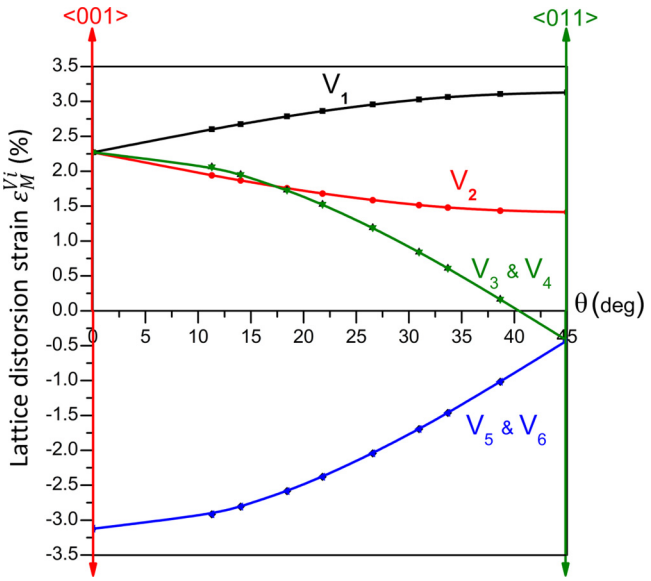

FIG. 7. Lattice distortion strains ε_M^{Vi} of each martensite variant *Vi* along selected β crystal directions as a function of θ angle between the selected x direction for ε_M^{Vi} calculations and $\langle 001\rangle_\beta$ direction.

direction by the following equation: $\varepsilon_M^{(Vi)} = \frac{|X'^{(Vi)}| - |X|}{|X|}$. As proposed by Tahara *et al.* [59], ε_M^{Vi} are calculated along various x directions of the β crystal for the six existing martensite variants. Results are shown in Fig. 7 as the function of the θ angle, which is defined as the angle between the selected x direction for $\varepsilon_M^{(Vi)}$ calculations and the $[001]_\beta$ direction (when $\theta = 0°$ or 45°, x direction is $[001]_\beta$ or $[011]_\beta$, respectively). Figure 7 evidences that the sign and magnitude of $\varepsilon_M^{(Vi)}$ depend significantly on *Vi* and θ. Martensite variant *V1* has the highest positive ε_M^{Vi} values whereas the largest negative $\varepsilon_M^{(Vi)}$ values are found for *V5* and *V6*. It is commonly assumed that the variant that would accommodate maximum strain along the direction of the applied load would produce maximum driving force for the martensitic transformation and would thus be preferentially formed. Thus $\varepsilon_M^{(Vi)}$ calculations predict the most favorable variant that is triggered to form first based on direction of the applied load and so predict maximum superelastic recovery accomodated from martensitic transformation for a defined loading direction. This indicates that *V1* is the most favorable variant upon tensile load and the maximum lattice distorsion strain for *V1* (3.1%) is obtained when tensile loading direction is parallel to $\langle 011\rangle_\beta$, also meaning that the largest superelastic strain recovery in tension is expected along the $\langle 011\rangle_\beta$ loading direction. Conversely, *V5* and *V6* are the most favorable variants for compressive loading situations and the maximum lattice distorsion strain for *V5* and *V6* (3.1%) is obtained when the compressive loading direction is parallel to $\langle 001\rangle_\beta$, meaning that the largest superelastic strain recovery in compression is expected along the $\langle 001\rangle_\beta$ loading direction. Figure 7 also shows asymetry between tensile and compressive transformation strains: in the case of the $\langle 011\rangle_\beta$ loading direction, large tensile strain ($\varepsilon_M^{(V1)} = 3,1\%$) is accomodated from martensitic tranformation whereas very limited strain ($\varepsilon_M^{(V5-V6)} = 0,5\%$) is accommodated in compression. Lattice distorsion strains $\varepsilon_M^{(Vi)}$ induced by martensitic transformation

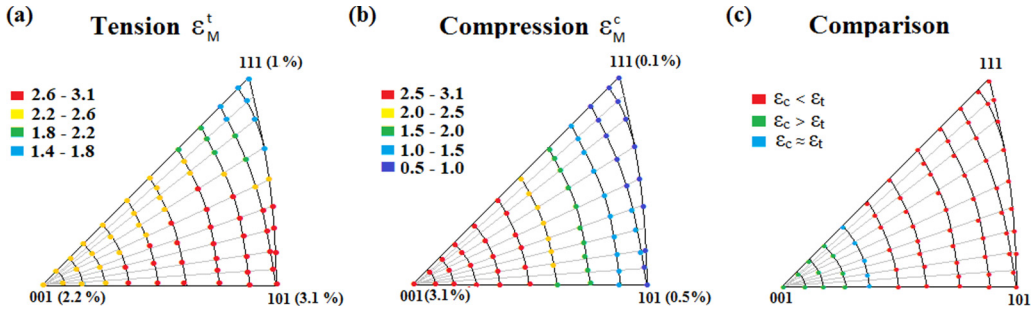

FIG. 8. Inverse pole figure distribution of maximum lattice distorsion strains ε_M-IPF that could be accomodated from martensitic transformation in single β grains under tension (a) and compression (b). Comparison of the maximum transformation strains ε_M between tension and compression (c).

in Ti2448 β crystals show thus strong orientation dependence. While reported values of lattice distorsion strain are only valid for the present Ti2448 alloy, the general tendancy highlighted here can be extended to all superelastic metastable β Ti-based alloys. To go further on this point, maximum lattice distorsion strains ε_M that can be accomodated from martensitic transformation regardless of the variants are reported in a standard stereographic triangle. The inverse pole figure distribution of maximum transformation strains ε_M-IPF is then presented for both tensile [Fig. 8(a)] and compressive [Fig. 8(b)] uniaxial deformation. A comparison between tensile and compressive maximum strains is also presented in Fig. 8(c), as previously proposed for Ni-Ti alloys by Mao *et al.* [52]. Maximum transformation strains under tension ε_M^t decrease with changing direction from $\langle 101\rangle_\beta$ toward the $\langle 001\rangle_\beta$ and $\langle 111\rangle_\beta$ directions, for which ε_M^t values are 3.1%, 2.2%, and 1.0%, respectively [Fig. 8(a)]. These findings are consistent with experimental observations upon uniaxial tensile testing of Ti2448 β single crystals [37]: a large-scale reversible strain of 4% has been measured along $\langle 101\rangle_\beta$ oriented single crystals, while $\langle 001\rangle_\beta$ and $\langle 111\rangle_\beta$ oriented single crystals exhibit lower values of 2.5% and 1.0%, respectively. Maximum transformation strains under compression ε_M^c evolve differently from those under tension: ε_M^c values decrease with changing direction from the $\langle 001\rangle_\beta$ toward $\langle 101\rangle_\beta$ and $\langle 111\rangle_\beta$ directions, for which ε_M^c values are 3.1%, 0.5%, and 0.1%, respectively [Fig. 8(b)]. Orientation dependence of maximum transformation strains under compression ε_M^c can be correlated with our indentation strain recovery ratios ε_{rec} measurements [Fig. 5(a)]: it is expected that the largest ε_M^c value calculated along the $\langle 001\rangle_\beta$ direction promotes the highest recoverable strain under compression and explains, in turn, the highest ε_{rec} measured in this direction under nanoindentation. Although nanoindentation test is different compared to uniaxial compression test, ε_{rec}-IPF and ε_M^c-IPF are in good qualitative agreement. Calculations and measurements follow the same trend $\varepsilon_{[001]\beta} > \varepsilon_{[101]\beta} > \varepsilon_{[111]\beta}$ supporting that nanoindentation, especially using spherical indenter, is a suitable technique to probe crystallographic anisotropy of superelastic response in β-Ti based alloys, which is mainly governed by orientation dependence of lattice distorsions induced during transformation from parent β crystal to martensite α" crystal. It appears that the strain induced under the spherical indenter is largely accommodated by the reversible stress-induced martensitic transformation leading to a remarkable superelastic strain recovery upon unloading whereas a significant volume of material directly below the Berkovich indenter is so highly stressed that most of the deformation occured by dislocation motion implying that this volume cannot contribute to the reversible stress-induced martensitic transformation causing an irretrievable loss of superelasticity [53,55–57]. The small differences in depth recovery depending on the loading direction for the Berkovich tip support that orientation effects are mainly governed by the stress-induced martensitic formation, which is considerably restricted during Berkovich indentations. It is also worth noting that in this study the large spherical tip (50 μm radius) is more appropriate to measure the recoverable strain anisotropy along one direction because the strain distribution under the spherical tip is much closer to an uniaxial compression configuration than that given by the Berkovich tip.

Transformation strain calculations show that Ti2448 crystals possess both anisotropic and asymmetric superelastic behavior (Fig. 8). Anisotropy refers to transformation strain changes with crystallographic loading direction, and asymmetry refers to difference in the magnitude of transformation strain between tension and compression for one loading direction. The asymmetry of recoverable strain between tensile and compressive uniaxial tests has been experimentally confirmed in Ti2448 single crystals at macroscale: $\langle 110\rangle_\beta$ oriented crystals exhibit larger reversible strain of 4% in tension whereas the reversible strain is considerably reduced (0.7%) under compression along the same crystal direction [37]. Most of the orientations show that $\varepsilon_M^t > \varepsilon_M^c$ [Fig. 8(c)] meaning there is a heightened probability of measuring a higher superelasticity in tension than in compression. This asymmetry has been also observed in polycrystalline Ti2448 alloy at macroscale with greater strain recovery in tension (3.3%) than in compression (1.3%) [60]. Our calculations and nanoindentation experiments assessed at submicrometer scale are thus consistent with macroscale mechanical tests available in the literature [37]. Clearly, calculations show that anisotropy of nanoindentation strain recovery ε_{rec} arises from orientation dependence of the formation of stress-induced martensite during nanoindentation into individual grains of the metastable β Ti2448 alloy.

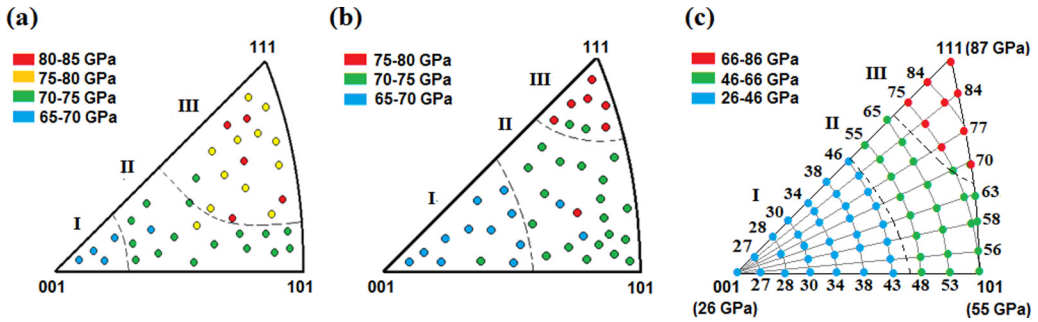

FIG. 9. Inverse pole figure distribution of indentation elastic modulus (E-IPF) measured with spherical tip (a), Berkovich tip (b), and calculated from Ti2448 elastic constants C_{ij} (c).

C. Anisotropy of the indentation modulus

The same strategy is conducted to characterize orientation dependence of the indentation elastic modulus. Inverse pole figure distribution of indentation modulus E-IPF is presented for both spherical testing [Fig. 9(a)] and Berkovich testing [Fig. 9(b)]. The indentation modulus clearly depends on crystallographic direction. The same trend is observed for the two indenter geometries: orientations around $\langle 001\rangle_\beta$ and $\langle 111\rangle_\beta$ have the minimum (65–70 GPa) and maximum (75–80 GPa) indentation modulus respectively, and $\langle 101\rangle_\beta$ orientation has values falling in the intermediate interval (70–75 GPa). The high statistic of measurements carried out along a large selection of crystallographic directions allowed an investigation through the entire fundamental stereographic triangle of the β phase [Figs. 9(a) and 9(b)]. Each colored point corresponds again to the average of at least five measurements and the mean standard deviation is 3 GPa. Anisotropy of the indentation modulus is supported by consistent values that change continuously through the fundamental triangle. It is well established that the orientation dependence of the elastic modulus is related to the anisotropy factor $A = 2C_{44}/(C_{11} - C_{12})$ of the crystal: any value of A either smaller or greater than unity gives the degree of elastic anisotropy possessed by the crystal. Elastic constants measured in Ti2448 single crystals by Zhang *et al.* [37] and the corresponding anisotropy factor are reported in Table II, with additional measured data from some other Ti-based cubic single crystals for comparison: Ti-29Nb-Ta-Zr [10], Ti-30Nb [61], and Ti-Ni alloys [62]. The anisotropy factor is much higher for Ti2448 alloy than for the quaternary and the binary Ti-based alloys referenced in Table II, indicating that a more prononced orientation dependence of elastic modulus is expected in the case of Ti2448 compared to other previously mentioned alloys.

TABLE II. Experimental elastic constants (C_{11}, C_{12}, C_{44}) and anisotropy factor (A) for Ti2448, Ti-29Nb-Ta-Zr (TNTZ), Ti-30Nb, and Ti-Ni crystals.

	C_{11} (GPa)	C_{12} (GPa)	C_{44} (GPa)	A
Ti2448[a]	57.2	36.1	35.9	3.4
TNTZ (Ti-29Nb-Ta-Zr)[b]	65.1	40.5	32.4	2.6
Ti-30Nb[c]	137.0	109.6	33.2	2.2
Ti-Ni[d]	130	98	34	2.1

[a]Reference [37].
[b]Reference [10].
[c]Reference [61].
[d]Reference [62].

The directional dependence of elastic modulus can be predicted in a cubic crystal using the following relation [63]:

$$E_{[hkl]} = \left\{ \frac{c_{11} + c_{12}}{(c_{11} - c_{12})(c_{11} + 2c_{12})} + \left(\frac{1}{c_{44}} - \frac{2}{c_{11} - c_{12}} \right)(h^2k^2 + k^2l^2 + l^2h^2) \right\}^{-1} \quad (4)$$

Elastic modulus values are then calculated from Ti2448 elastic constants [37] and are finally reported in the stereographic fundamental triangle of the β phase [Fig. 9(c)]. The calculated E-IPF also exhibits significant anisotropy: orientations around $\langle 001\rangle_\beta$ and $\langle 111\rangle_\beta$ have the minimum (26 GPa) and maximum (87 GPa) elastic modulus, respectively. The elastic response of individual grains of Ti2448 to nanoindentation as well as the elastic response of Ti2448 single crytals to resonant methods [37], follow the sequence predicted by calculations: $E_{[001]\beta} < E_{[101]\beta} < E_{[111]\beta}$, i.e., $\langle 001\rangle_\beta$ orientation as the most compliant direction and $\langle 111\rangle_\beta$ orientation as the stiffest direction. E-IPF experimentally achieved at a submicrometer scale using nanoindentation [Figs. 9(a) and 9(b)] are then in good agreement with calculated E-IPF [Fig. 9(c)] and with previous determination of elastic properties using resonnant methods in Ti2448 single crystals [37].

To assist in the discussion, E-IPF are divided into three regions, each region referring to distinct interval values (Fig. 9). For regions I and II, a clear difference is observed between elastic moduli assessed at the submicrometer scale using nanoindentation, ranging from 65 to 75 GPa [Figs. 9(a) and 9(b)], and the ones calculated [Fig. 9(c)] or measured by vibratory motion [37], ranging from 26 to 66 GPa. Elastic moduli determined by nanoindentation appear overestimated compared to those calculated from measured elastic constants or obtained by vibratory motion. This is explained by the fact that the true contact area can be underestimated during indentation leading to overestimation of the indentation modulus, which is consistent with the literature [64,65]. Accurate determination of the contact area during post-experiment using imaging techniques can be used only if elastic recovery is negligible, which is not the present case. The spatial distribution of region I becomes much smaller when the spherical

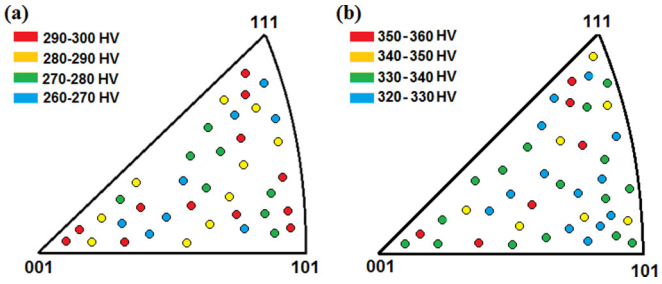

FIG. 10. Inverse pole figure distribution of hardness measurements (H-IPF) with spherical tip (a) and with Berkovich tip (b).

tip is employed. One suggestion for this effect is that spherical indentation promotes stress-induced martensite formation for which martensite is known to have a higher elastic modulus than the β phase [66]. Indeed, as the modulus is measured from the onset of the unloading nanoindentation curve, both β and α'' phases contribute to the measured value, which is the source of the stiffening under the spherical tip. In contrast, the spatial distribution of regions I, II, and III in the E-IPF determined from Berkovich experiments is similar to that obtained by calculations. Plastic deformation is the predominant deformation mechanism during Berkovich nanoindentation and the high deformation field promptly developed underneath this sharp indenter cannot be accommodated by martensitic transformation. Therefore, the Berkovich indenter tip seems the most appropriate indenter to probe conventional elastic properties of our plastically deformed Ti2448 alloy.

D. Indentation hardness

Inverse pole figure distributions of hardness (H-IPF) obtained from spherical and Berkovich nanoindentations are presented in Figs. 10(a) and 10(b), respectively. Each colored point corresponds again to the average of at least five measurements and the mean standard deviation is 18 GPa. No significant change in hardness values is found with crystallographic orientation for both tips. It means that whatever the orientation of the grain, hardness remains unchanged in the range of dispersion of the measurements. Similar results have been highlighted in polycrystalline α/β Ti alloys [67]. These results are contrary to measurements in pure α Ti for which a strong anisotropy of hardness has been measured from nanoindention experiments [40]. This observation is due to a strong anisotropy of slip systems in α Ti resulting from its hcp structure. Indeed, easy slip activation is allowed only for the three prismatic slip systems leading thus to high hardness values for crystallographic orientations around $[0001]_\alpha$ that are unfavorable for prismatic slip systems. Contrarily, β Ti alloys always possess slip systems easy to be activated whatever the crystallographic direction. This is due to the combination of the cubic symetry, which is more isotropic than a hexagonal one and the high number of potential slip systems. Indeed, as with most bcc metals and alloys, dislocation slip can be easily activated in both the {110} and {112} planes [68]. But in β Ti alloys, dislocation activity is also found to be easy in the {123} planes for crystallographic orientation less favorable to {110} and {112} slip systems [69–72]. Therefore, this feature allows dislocation slip to be activated rather easily for any crystallographic orientation and supports the isotropic distribution of hardness values usually observed in bcc alloys.

We should like to emphasize that approximately linear relationships between the ratio of hardness to elastic modulus and the ratio of irreversible work to total work in indentation have been proposed in the literature for Berkovich and spherical indentations in elastic-plastic solids [73–75]. The ratio values $H_{\text{ind}}/E^* \approx 0.045 - 0.047$ and $(W_{\text{total}} - W_{\text{rec}})/W_{\text{total}} \approx 0.70 - 0.72$ measured in our Ti2448 with Berkovich indenter follow the linear relationship established for Berkovich indentations in elastic-plastic solids [73,74], once again indicating that Berkovich indentations favor elastic-plastic deformation. Indeed, the ratio values $H_{\text{ind}}/E^* \approx 0.032 - 0.037$ and $(W_{\text{total}} - W_{\text{rec}})/W_{\text{total}} \approx 0.32 - 0.41$ measured in our Ti2448 with the spherical indenter deviate from the linear relationship governing the work done during spherical indentation in elastic-plastic solids [75]. The deviation is attributed to the contribution of the superelastic recovery (martensite to β back transformation during unloading) in the specific case of superelastic alloys, in addition to the classical elastic recovery, leading to a considerably higher work recovery ratio during spherical indentations.

IV. CONCLUSIONS

The dependence of crystallographic orientation on the mechanical response in individual grains of superelastic polycrystalline Ti2448 alloy is investigated during nanoindentation. Strain recovery, elastic modulus, and hardness are evaluated from the force-displacement curves using spherical and Berkovich indenters. The strain recovery, defined as the indentation depth-recovery ratio, is strongly affected by crystallographic indentation direction and reaches a maximum value along the $\langle 001 \rangle_\beta$ direction and a minimum value along the $\langle 111 \rangle_\beta$ direction. The IPF distributions of indentation strain recoveries are in good agreement with the IPF distribution of compressive lattice distorsions calculated from the crystallographic model of martensitic transformation evidencing that anisotropy of indentation strain recovery arises from the superelastic nature of our alloy. This interpretation is further supported by the fact that maximum penetration depths and hardness (resistance to plastic deformation) measured in this study are clearly not affected by crystallographic loading direction and can therefore not be responsible for orientation effects. These IPF distributions are very different from that calculated for tensile deformation, and both our experiments and calculations confirm the strong tension-compression asymmetry of the recoverable strain in superelastic β Ti alloys. The present study attests that the orientation dependence of the superelastic effect can be probed from nanoindentation experiments in individual grains of the superelastic polycrystalline Ti2448 alloy, and higher sensitivity is obtained with the spherical indenter tip. The strain distribution induced under the spherical indenter can be largely accommodated by stress-induced martensitic transformation, leading to reversible phase transformation from martensite to β phase upon unloading resulting in notable superelastic strain recovery. The indentation modulus also shows significant dependence on crystal orientation in agreement with measured

values in single crystals of Ti2448 subjected to tensile deformation: $E_{[001]\beta} < E_{[101]\beta} < E_{[111]\beta}$. The IPF distributions of the indentation modulus are qualitatively similar to the one predicted by calculations of elastic modulus from Ti2448 elastic constants. Calculations also show that the Berkovich indenter tip is more suitable for probing anisotropy of elastic properties in superelastic alloys. Our results show that crystallographic anisotropy of the nanoindentation response is governed by anisotropy of elastic and superelastic responses in our metastable β Ti2448 alloy. In contrast, orientation dependence is lost when plasticity has set in, and no crystallographic anisotropy of hardness is detected due to the fact that multiple directions are prone to generate slip systems in the bcc-β phase.

[1] C. Leyens and M. Peters, *Titanium and Titanium Alloys: Fundamentals and Applications* (WILEY-VCH Verlag, New York, 2003).

[2] Y. Oshida, *Bioscience and Bioengineering of Titanium Materials*, 2nd ed (Elsevier Science Inc., 2012).

[3] X. Liu, P. K. Chu, and C. Ding, Mater. Sci. Eng. R **47**, 49 (2004).

[4] D. R. Sumner, T. M. Turner, R. Igloria, R. M. Urban, and J. O. Galante, J. Biomech. **31**, 909 (1998).

[5] T. Ozaki, H. Matsumoto, S. Watanabe, and S. Hanada, Mater. Trans. **45**, 2776 (2004).

[6] M. Niinomi, Biomaterials **24**, 2673 (2003).

[7] H. Y. Kim, S. Hashimoto, J. I. Kim, H. Hosoda, and S. Miyazaki, Mater. Trans. **45**, 2443 (2004).

[8] Y. L. Hao, S. J. Li, S. Y. Sun, C. Y. Zheng, Q. M. Hu, and R. Yang, Appl. Phys. Lett. **87**, 091906 (2005).

[9] Y. L. Hao, S. J. Li, S. Y. Sun, C. Y. Zheng, and R. Yang, Acta Biomater. **3**, 277 (2007).

[10] M. Tane, S. Akita, T. Nakano, K. Hagihara, Y. Umakoshi, M. Niinomi, and H. Nakajima, Acta Mater. **56**, 2856 (2008).

[11] M. Geetha, A. K. Singh, R. Asokamani, and A. K. Gogia, Prog. Mater. Sci. **54**, 397 (2009).

[12] M. Niinomi, J. Mech. Behav. Biomed. Mater. **1**, 30 (2008).

[13] Y. Guo, K. Georgarakis, Y. Yokoyama, and A. R. R. Yavari, J. Alloys Compd. **571**, 25 (2013).

[14] S. Miyazaki, H. Y. Kim, and H. Hosoda, Mater. Sci. Eng. A **438–440**, 18 (2006).

[15] W. Elmay, E. Patoor, T. Gloriant, F. Prima, and P. Laheurte, J. Mater. Eng. Perform. **23**, 2471 (2014).

[16] H. Y. Kim, Y. Ikehara, J. I. Kim, T. Inamura, H. Hosoda, and S. Miyazaki, Acta Mater. **54**, 2419 (2006).

[17] Y. L. Hao, S. J. Li, S. Y. Sun, and R. Yang, Mater. Sci. Eng. A **441**, 112 (2006).

[18] T. Gloriant, G. Texier, F. Prima, D. Laille, D. M. Gordin, I. Thibon, and D. Ansel, Adv. Eng. Mater. **8**, 961 (2006).

[19] F. Sun, Y. L. Hao, S. Nowak, T. Gloriant, P. Laheurte, and F. Prima, J. Mech. Behav. Biomed. Mater. **4**, 1864 (2011).

[20] T. Duerig, A. Pelton, and D. Stockel, Mater. Sci. Eng. A **273–275**, 149 (1999).

[21] T. Hanawa, J. Artif. Organs **12**, 73 (2009).

[22] C. J. Burstone and A. J. Goldberg, Am. J. Orthod. **77**, 121 (1980).

[23] F. EI Feninat, G. Laroche, M. Fiset, and D. Mantovani, Adv. Eng. Mater. **4**, 91 (2002).

[24] E. Takahashi, T. Sakurai, S. Watnabe, N. Masahashi, and S. Hanada, Mater. Trans. **43**, 2978 (2002).

[25] J. Y. Zhang, F. Sun, Y. L. Hao, N. Gazdecki, E. Leburn, P. Vermaut, R. Portier, T. Gloraint, P. Laheurte, and F. Prima, Mater. Sci. Eng. A **563**, 78 (2013).

[26] I. M. Farzik, H. Y. Kim, H. Hosoda, and S. Miyazaki, Mater. Sci. Eng. C **48**, 11 (2015).

[27] L. L. Pavón, H. Y. Kim, H. Hosoda, and S. Miyazaki, Scr. Mater. **95**, 46 (2015).

[28] I. M. Farzik, H. Y. Kim, H. Hosoda, and S. Miyazaki, Scr. Mater. **72-73**, 29 (2014).

[29] Y. F. Xu, D. Q. Yi, H. Q. Liu, X. Y. Wu, B. Wang, and F. L. Yang, Mater. Sci. Eng. A **547**, 64 (2012).

[30] H. Y. Kim, T. Sasaki, K. Okutsu, J. I. Kim, T. Inamura, H. Hosoda, and S. Miyazaki, Acta Mater. **54**, 423 (2006).

[31] Y. Yang, P. Castany, M. Cornen, I. Thibon, F. Prima, and T. Gloriant, J. Alloys Compd. **591**, 85 (2014).

[32] A. Ramarolahy, P. Castany, F. Prima, P. Laheurte, I. Péron, and T. Gloriant, J. Mech. Behav. Biomed. Mater. **9**, 83 (2012).

[33] F. Sun, S. Nowak, T. Gloriant, P. Laheurte, A. Eberhardt, and F. Prima, Scr. Mater. **63**, 1053 (2010).

[34] H. Matsumoto, S. Watanabe, and S. Hanada, J. Alloys Compd. **439**, 146 (2007).

[35] M. J. Xiao, Y. X. Tian, G. W. Mao, S. J. Li, Y. L. Hao, and R. Yang, J. Mater. Sci. Tech. **27**, 1099 (2011).

[36] Q. Meng, Q. Liu, S. Guo, Y. Zhu, and X. Zhao, Prog. Nat. Sci. Mater. Int. **25**, 229 (2015).

[37] Y. W. Zhang, S. J. Li, E. G. Obbard, H. Wang, S. C. Wang, Y. L. Hao, and R. Yang, Acta Mater. **59**, 3081 (2011).

[38] S. H. Lee, M. Todai, M. Tane, K. Hagihara, H. Nakajima, and T. Nakano, J. Mech. Behav. Biomed. Mater. **14**, 48 (2012).

[39] X. Wang, L. Zhang, Z. Guo, Y. Jiang, X. Tao, and L. Liu, J. Mech. Behav. Biomed. Mater. **62**, 310 (2016).

[40] C. Fizanne-Michel, M. Cornen, P. Castany, I. Péron, and T. Gloriant, Mater. Sci. Eng. A **613**, 159 (2014).

[41] E. Merson, R. Brydson, and A. Brown, J. Phys.: Conf. Series **126**, 012020 (2008).

[42] C. Tromas, J. C. Stinville, C. Templier, and P. Villechaise, Acta Mater. **60**, 1975 (2012).

[43] R. D. Dar and Y. Chen, Acta Mater. **91**, 112 (2015).

[44] J. C. Stinville, C. Tromas, P. Villechaise, and C. Templier, Scr. Mater. **64**, 37 (2011).

[45] C. P. Frick, S. Orso, and E. Arzt, Acta Mater. **55**, 3845 (2007).

[46] C. P. Frick, B. G. Clark, S. Orso, P. Sonnweber-Ribic, and E. Arzt, Scr. Mater. **59**, 7 (2008).

[47] J. Pfetzing-Micklich, R. Ghisleni, T. Simon, C. Somsen, J. Michler, and G. Eggeler, Mater. Sci. Eng. A **538**, 265 (2012).

[48] J. Pfetzing-Micklich, C. Somsen, A. Dlouhy, C. Begau, A. Hartmaier, F. Martin, X. Wagner, and G. Eggeler, Acta Mater. **61**, 602 (2013).

[49] G. Laplanche, J. Pfetzing-Micklich, and G. Eggeler, Acta Mater. **68**, 19 (2014).

[50] G. Laplanche, J. Pfetzing-Micklich, and G. Eggeler, Acta Mater. **78**, 144 (2014).

[51] S. C. Mao, J. F. Luo, Z. Zhang, M. H. Wu, Y. Liu, and X. D. Han, Acta Mater. **58**, 3357 (2010).
[52] W. C. Oliver and G. M. Pharr, J. Mater. Res. **7**, 1564 (1992).
[53] W. Ni, Y. T. Cheng, and D. S. Grummon, Appl. Phys. Lett. **82**, 2811 (2003).
[54] See Supplemental Material at http://link.aps.org/supplemental/10.1103/PhysRevMaterials.3.063608 for raw load-displacement data measured during nanoindentation tests.
[55] G. Pan, Z. Cao, J. Shi, M. Wei, L. Xu, and X. Meng, Sens. Actuators A **217**, 75 (2014).
[56] J. Pfetzing-Micklich, M. F.-X. Wagner, R. Zarnetta, J. Frenzel, G. Eggeler, A. E. Markaki, J. Wheeler, and T. W. Clyne, Adv. Eng. Mater. **12**, 13 (2010).
[57] Y. Zhang, Y. T. Cheng, and D. S. Grummon, J. Appl. Phys. **101**, 053507 (2007).
[58] Y. Yang, P. Castany, M. Cornen, F. Prima, S. J. Li, Y. L. Hao, and T. Gloriant, Acta Mater. **88**, 25 (2015).
[59] M. Tahara, H. Y. Kim, T. Inamura, H. Hosoda, and S. Miyazaki, Acta Mater. **59**, 6208 (2011).
[60] Z. B. Zhang, Y. L. Hao, S. J. Li, and R. Yang, Mater. Sci. Eng. A **577**, 225 (2013).
[61] R. Hermann, H. Hermann, M. Calin, B. Büchner, and J. Eckert, Scr. Mater. **66**, 198 (2012).
[62] S. Manchiraju and P. M. Anderson, Int. J. Plastic. **26**, 1508 (2010).
[63] A. Cazzani and M. Rovati, Int. J. Solid. Struct. **40**, 1713 (2003).
[64] R. A. Mirshams and R. M. Pothapragada, Acta Mater. **54**, 1123 (2006).
[65] G. B. Viswanathan, E. Lee, D. M. Maher, S. Banerjee, and H. L. Fraser, Acta Mater. **53**, 5101 (2005).
[66] E. Bertrand, T. Gloriant, D. M. Gordin, E. Vasilescu, P. Drob, C. Vasilescu, and S. I. Drob, J. Mech. Behav. Biomed. Mater. **3**, 559 (2010).
[67] X. Lei, L. Dong, Z. Zhang, M. Hu, Z. Wang, Y. Hao, and R. Yang, Sci. Adv. Mater. **9**, 1476 (2017).
[68] J. Christian, Metall. Mater. Trans. A **14**, 1237 (1983).
[69] P. Castany, M. Besse, and T. Gloriant, Phys. Rev. B **84**, 020201(R) (2011).
[70] M. Besse, P. Castany, and T. Gloriant, Acta Mater. **59**, 5982 (2011).
[71] P. Castany, M. Besse, and T. Gloriant, Scr. Mater. **66**, 371 (2012).
[72] P. Castany, D. M. Gordin, S. I. Drob, C. Vasilescu, V. Mitran, A. Cimpean, and T. Gloriant, Shape Mem. Superelastic. **2**, 18 (2016).
[73] Y. T. Cheng and C. M. Cheng, Appl. Phys. Lett. **73**, 614 (1998).
[74] R. Yang, T. Zhang, P. Jiang, and Y. Bai, Appl. Phys. Lett. **92**, 231906 (2008).
[75] W. Ni, Y.-T. Cheng, C.-M. Chen, and D. S. Grummon, J. Matter. Res. **19**, 149 (2004).